

Late-time HST and JWST Observations of GRB 221009A: Evidence for a Break in the Light Curve at 50 days

Huei Sears^{1,18} , Ryan Chornock² , Peter K. Blanchard^{3,4} , Raffaella Margutti^{2,5} , V. Ashley Villar^{3,4} , Justin Pierel^{6,16} , Patrick J. Vallely⁷ , Kate D. Alexander⁸ , Edo Berger^{3,4} , Tarraneh Eftekhari^{9,16} , Wynn V. Jacobson-Galán^{10,17} ,

Tanmoy Laskar^{11,12} , Natalie LeBaron² , Brian D. Metzger^{13,14} , and Dan Milisavljevic¹⁵ 

¹ Department of Physics and Astronomy, Rutgers, the State University of New Jersey, 136 Frelinghuysen Road, Piscataway, NJ 08854-8019, USA

² Department of Astronomy, University of California, Berkeley, CA 94720-3411, USA

³ Center for Astrophysics | Harvard & Smithsonian, 60 Garden Street, Cambridge, MA 02138-1516, USA

⁴ The NSF AI Institute for Artificial Intelligence and Fundamental Interactions, USA

⁵ Department of Physics, University of California, 366 Physics North MC 7300, Berkeley, CA 94720, USA

⁶ Space Telescope Science Institute, Baltimore, MD 21218, USA

⁷ Core Pricing Systems, CarMax, Inc., Richmond, VA 23238, USA

⁸ Steward Observatory, University of Arizona, 933 North Cherry Avenue, Tucson, AZ 85721-0065, USA

⁹ Center for Interdisciplinary Exploration and Research in Astronomy (CIERA), Northwestern University, 1800 Sherman Avenue, Evanston, IL 60201, USA

¹⁰ Department of Astronomy and Astrophysics, California Institute of Technology, Pasadena, CA 91125, USA

¹¹ Department of Physics & Astronomy, University of Utah, Salt Lake City, UT 84112, USA

¹² Department of Astrophysics/IMAPP, Radboud University, P.O. Box 9010, 6500 GL, Nijmegen, The Netherlands

¹³ Department of Physics and Columbia Astrophysics Laboratory, Columbia University, New York, NY 10027, USA

¹⁴ Center for Computational Astrophysics, Flatiron Institute, 162 5th Ave, New York, NY 10010, USA

¹⁵ Department of Physics and Astronomy, Purdue University, 525 Northwestern Ave, West Lafayette, IN 47907, USA

Received 2024 December 3; revised 2025 March 17; accepted 2025 March 18; published 2025 May 9

Abstract

GRB 221009A is one of the brightest transients ever observed, with the highest peak gamma-ray flux for a gamma-ray burst (GRB). A Type Ic-BL supernova (SN), SN 2022xiw, was definitively detected in late-time JWST spectroscopy ($t = 195$ days, observer frame). However, photometric studies have found SN 2022xiw to be less luminous (10%–70%) than the canonical GRB-SN, SN 1998bw. We present late-time Hubble Space Telescope (HST)/WFC3 and JWST/NIRCam imaging of the afterglow and host galaxy of GRB 221009A at $t \sim 185$, 277, and 345 days post-trigger. Our joint archival ground, HST, and JWST light-curve fits show strong support for a break in the light-curve decay slope at $t = 50 \pm 10$ days (observer frame) and a SN at $< 1.5 \times$ the optical/near-IR flux of SN 1998bw. This break is consistent with an interpretation as a jet break when requiring slow-cooling electrons in a wind medium with an electron energy spectral index $p > 2$ and $\nu_m < \nu_c$. Our light curves and joint HST/JWST spectral energy distribution (SED) also show evidence for the late-time emergence of a bluer component in addition to the fading afterglow and SN. We find consistency with the interpretations that this source is either a young, massive, low-metallicity star cluster or a scattered-light echo of the afterglow with a SED shape of $f_\nu \propto \nu^{2.0 \pm 1.0}$.

Unified Astronomy Thesaurus concepts: Gamma-ray bursts (629); Core-collapse supernovae (304); Supernovae (1668); High energy astrophysics (739); HST photometry (756); Hubble Space Telescope (761); James Webb Space Telescope (2291)

1. Introduction

Gamma-ray bursts (GRBs) are some of the most energetic and luminous events in the Universe. The brightest GRBs usually have gamma-ray (~ 1 –10,000 keV) fluences on the order of 10^{-3} erg cm $^{-2}$ and peak fluxes on the order of 10^{-4} erg s $^{-1}$ cm $^{-2}$ (see Tables 2 and 3 of E. Burns et al. 2023). GRBs are also measured to have typical gamma-ray isotropic energies ($E_{\gamma, \text{iso}}$) on the order of 10^{53} erg (D. A. Frail et al. 2001; M. Ajello et al. 2019) and isotropic luminosities on the order of 10^{53} erg s $^{-1}$ (L. Nava et al. 2012; B. P. Abbott et al. 2017; A. Tsvetkova et al. 2017; E. Burns et al. 2023).

GRB 221009A was discovered on 2022 October 9, 13:17:00 UT by the Fermi Gamma-ray Burst Monitor (P. Veres et al. 2022;

E. Burns et al. 2023; S. Lesage et al. 2023) and soon after by the Swift Burst Alert Telescope (S. Dichiara et al. 2022; M. A. Williams et al. 2023). This GRB was detected to have a gamma-ray fluence of 0.19 erg cm $^{-2}$, a peak flux of 0.01 erg s $^{-1}$ cm $^{-2}$, a gamma-ray isotropic energy of $E_{\gamma, \text{iso}} = 10^{55}$ erg, and a peak isotropic-equivalent luminosity of $\sim 10^{54}$ erg s $^{-1}$ (E. Burns et al. 2023; S. Lesage et al. 2023). This is the highest recorded gamma-ray fluence, $E_{\gamma, \text{iso}}$, and peak flux, and is only superseded in isotropic-equivalent luminosity by two GRBs (E. Burns et al. 2023). The GRB has low Galactic latitude, $b = 4^\circ 3$ (M. A. Williams et al. 2023), and suffers from high Galactic extinction, $A_V \sim 4.2$ mag (E. F. Schlafly & D. P. Finkbeiner 2011). Despite this, the multiwavelength afterglow was detected by a variety of observatories, allowing for several extensive follow-up campaigns (Y. Huang et al. 2022; J. S. Bright et al. 2023; M. D. Fulton et al. 2023; T. Laskar et al. 2023; A. J. Levan et al. 2023; LHAASO Collaboration et al. 2023; M. Negro et al. 2023; B. O'Connor et al. 2023; M. Shrestha et al. 2023; G. P. Srinivasaragavan et al. 2023; P. K. Blanchard et al. 2024; D.-F. Kong et al. 2024; L. Rhodes et al. 2024), and a redshift of $z = 0.151$ was determined from

¹⁶ NHFP Einstein Fellow.

¹⁷ NHFP Hubble Fellow.

¹⁸ Corresponding author.

Very Large Telescope/X-Shooter spectroscopy of the afterglow (A. de Ugarte Postigo et al. 2022a; D. B. Malesani et al. 2023).

Several previous studies presented synchrotron models of the afterglow (J. S. Bright et al. 2023; M. D. Fulton et al. 2023; E. Guarini et al. 2023; T. Laskar et al. 2023; A. J. Levan et al. 2023; J. Ren et al. 2023; Y. Sato et al. 2023; L. Rhodes et al. 2024; D. Tak et al. 2025). In the synchrotron emission model, the GRB afterglow is initially expected to decay as a power law in flux versus time. There is predicted to be at least one luminosity break in the light curve, called a “jet break,” which manifests as a steeper power-law decay in flux versus time. This break is due to relativistic beaming and the jetted nature of the source. The break time depends on the physical geometry (i.e., the jet opening angle, θ_{jet} , and the viewing angle); the intrinsic kinetic energy, E_k (which can be parameterized to $E_{\gamma,\text{iso}}$ with assumptions about the energy efficiency of the GRB); the circumstellar density; and the density profile of the circumburst medium (J. E. Rhoads 1999; R. Sari et al. 1999; R. A. Chevalier & Z.-Y. Li 2000; D. A. Frail et al. 2001; J. S. Bloom et al. 2003; S.-X. Yi et al. 2015). Furthermore, the opening angle and the isotropic energy can be used to calculate the true gamma-ray energy release of the jet via $E_{\gamma} = E_{\gamma,\text{iso}}(1 - \cos(\theta_{\text{jet}}))$. The superlatively high $E_{\gamma,\text{iso}}$ inferred from the gamma-ray prompt emission (Z.-H. An et al. 2023; E. Burns et al. 2023; D. Frederiks et al. 2023; S. Lesage et al. 2023) suggests a small jet opening angle (and therefore a small jet break time or dense circumburst medium) for realistic calculations of E_{γ} . P. D’Avanzo et al. (2022) and M. Shrestha et al. (2023) reported evidence for a jet break at $t \sim 1$ day (observer frame). A. J. Levan et al. (2023) presented observations which were interpreted to require a jet break at $t < 0.03$ days (observer frame), in conflict with a jet break at $t \sim 1$ day. T. Laskar et al. (2023) present a forward-shock synchrotron model that can moderately explain the optical to X-ray data but cannot explain the radio and predicts a jet break at $t \sim 100$ days. More data at later times and complete, multi-wavelength light-curve fitting is needed to resolve the seemingly conflicting results in many of these early works.

Collapsar-caused long GRBs are expected to be followed by a Type Ic-BL supernova (SN; S. E. Woosley & J. S. Bloom 2006). For events that are sufficiently nearby ($z \lesssim 0.1$), almost all long GRBs have proven this expectation true. There are some exceptions to this, e.g., GRBs 230307A (J. H. Gillanders et al. 2023; A. J. Levan et al. 2024; Y.-H. Yang et al. 2024), 211211A (J. C. Rastinejad et al. 2022; E. Troja et al. 2022; B. P. Gompertz et al. 2023), 111005A (Y.-Z. Wang et al. 2017; M. J. Michałowski et al. 2018; M. Tanga et al. 2018), 060614A (M. Della Valle et al. 2006; J. P. U. Fynbo et al. 2006; A. Gal-Yam et al. 2006; N. Gehrels et al. 2006), and 060605A (J. P. U. Fynbo et al. 2006; E. O. Ofek et al. 2007), which may arise from merger events. The first long GRB to have an observed SN was GRB 980425/SN 1998bw ($z = 0.0085$, though some now consider this GRB an X-ray flash; T. J. Galama et al. 1998; G. Ghisellini et al. 2006; F. J. Virgili et al. 2009). SN 1998bw has extensive multi-wavelength photometry and spectroscopy to late times, $t \sim 400$ days (rest frame) post-trigger, that are used to model other SNe associated with GRBs (GRB-SNe).

In the case of GRB 221009A, there have been several searches for an associated SN; however, many studies were only able to place upper limits on its luminosity (T. Laskar et al. 2023; A. J. Levan et al. 2023; M. Shrestha et al. 2023) or found weak evidence for a SN detection (SN 2022xiw;

A. de Ugarte Postigo et al. 2022b; E. Maiorano et al. 2022; M. D. Fulton et al. 2023; D.-F. Kong et al. 2024). The SN was finally confidently identified with a JWST/NIRSpec spectrum at 194 days (observer frame) post-trigger (P. K. Blanchard et al. 2024).

To further constrain the properties of the afterglow and SN, we continued to monitor the light curve with HST and JWST. Here, we present late-time ($t = 185$ –345 days, observer frame) HST/WFC3 and JWST/NIRCam imaging of the host and afterglow of GRB 221009A. In Section 2, we describe the observations. In Section 3, we describe the data reduction and photometric measurement steps. In Section 4, we discuss the interpretation of the spectral energy distribution (SED) and light curve of the afterglow. We discuss the evidence for a constant, blue component in addition to the afterglow and our detection of a break at $t \sim 50$ days, which is consistent with an interpretation as a jet break. We conclude with comparisons to the larger GRB sample of jet-break times and optical light curves. All times are presented in the observer frame, unless otherwise expressly noted. Days since trigger are measured from the Fermi trigger of 2022 October 9, 13:17:00 UT (S. Lesage et al. 2023). We use a cosmological model with $H_0 = 68 \text{ km s}^{-1} \text{ Mpc}^{-1}$, $\Omega_0 = 0.31$, and $\Omega_{\Lambda} = 0.69$.

2. Observations

2.1. Hubble Space Telescope

We obtained observations of the afterglow with HST/WFC3 (program GO-17278, PI: Chornock; R. Chornock et al. 2022) on 2023 April 12 (F110W, F160W; $\Delta t = 185.19$ days), 2023 July 13 (F814W, F110W, F160W; $\Delta t_{\text{F814W}} = 277.01$ days, $\Delta t_{\text{F110W},\text{F160W}} = 277.11$ days), 2023 September 2 (F814W; $\Delta t = 328.21$ days), 2023 September 3 (F110W, F160W; $\Delta t = 328.83$ days), and 2023 October 6 (F110W, F160W; $\Delta t = 361.93$ days). Loss of tracking due to loss of the guide star occurred in one of the 2023 September 3 orbits, and images were retaken on 2023 October 6. We also include HST/WFC3 F160W observations of this source from 2023 September 11 (program GO/DD 17264, PI: Levan; $\Delta t = 336.79$ days; A. J. Levan et al. 2022). We combine the 2023 September 3, 2023 September 11, and 2023 October 6 data into single-epoch images for F110W and F160W ($\Delta t_{\text{F160W}} = 342$ days, $\Delta t_{\text{F110W}} = 345$ days). We further refer to the imaging from 2023 April as “V1,” 2023 July as “V2,” and 2023 September (or otherwise combined) as “V3” (Table 1).

We use standard STScI software TweakReg and Astro-Drizzle to align and drizzle the images. We first use TweakReg to align the images to within one HST pixel. In AstroDrizzle, we use `final_scale = 0.065` for F110W and F160W and `final_scale = 0.02` for F814W imaging. The `final_pixfrac`, the fraction by which the input pixel is shrunk before being input onto the final grid, was maximized for each image following STScI recommended guidance that the standard deviation divided by the mean of the “wht” image was less than 0.20.¹⁹

2.2. JWST

P. K. Blanchard et al. (2024) present JWST observations at $\Delta t = 194.74$ days post-burst, roughly contemporaneous with

¹⁹ <https://hst-docs.stsci.edu/drizzpac/chapter-6-reprocessing-with-the-drizzpac-package/6-3-running-astrodrizzle>

Table 1
Photometry of the Afterglow of GRB 221009A

Filter and Visit	UT Date	Δt (days)	Measured Mag. (mag)	Measured Unc. (mag)	Systematic Unc. (mag)	Combined Unc. (mag)
HST						
F110W V1	2023 Apr 12	185.19	24.95	0.05	0.09	0.10
F110W V2	2023 Jul 13	277.11	25.68	0.11	0.10	0.15
F110W V3	2023 Sep 19 ^a	345	26.10	0.13	0.11	0.17
F160W V1 (GF)	2023 Apr 12	185.19	24.67	0.08	0.10	0.13
F160W V1 (HP)	2023 Apr 12	185.19	24.37	0.07	0.10	0.12
F160W V2	2023 Jul 13	277.11	25.01	0.11	0.15	0.19
F160W V3	2023 Sep 16 ^b	342	25.51	0.12	0.24	0.27
F814W V2	2023 Jul 13	277.01	27.00	0.05	0.11	0.12
F814W V3	2023 Sep 2	328.21	27.10	0.05	0.12	0.13
JWST						
F115W V1	2023 Apr 22	194.74	24.93	0.03	0.05	0.06
F200W V1	2023 Apr 22	194.74	24.05	0.02	0.05	0.06
F277W V1	2023 Apr 22	194.74	23.62	0.04	0.05	0.06
F444W V1	2023 Apr 22	194.74	23.11	0.04	0.05	0.06
F115W V3	2023 Sep 4	330.26	26.29	0.15	0.10	0.18
F200W V3	2023 Sep 4	330.26	25.22	0.07	0.10	0.12
F277W V3	2023 Sep 4	330.26	24.63	0.15	0.10	0.18
F444W V3	2023 Sep 4	330.26	24.18	0.14	0.10	0.17

Notes. Columns, from left to right. Column (1): the filter and visit, with visit designations as described in Section 2. Column (2): date of observations. Column (3): number of days after the trigger. Column (4): measured afterglow magnitude. Column (5): measured uncertainty of the afterglow magnitude. Column (6): systematic uncertainty of the afterglow magnitude. Column (7): the combined uncertainty, which is the quadrature sum of the measured and systematic uncertainties. The “GF” and “HP” designations refer to our choice of using GALFIT or HOTPANTS, respectively, to measure the photometry (see Section 3.2). The systematic uncertainty measurement procedure is detailed in Section 3.3.

^a These data were compiled from observations on 2023 September 3 and 2023 October 6.

^b These data were compiled from observations on 2023 September 3, 2023 September 11, and 2023 October 6.

HST V1 ($\Delta t = 185.19$ days, a 10 day offset). We present additional JWST/NIRCam imaging (ID: 2784, PIs: Blanchard, Chornock, Villar; P. Blanchard et al. 2022) from 2023 September 4 (F115W, F200W, F227W, F444W; $\Delta t = 330.26$ days). We follow similar reduction and analysis procedures as presented in P. K. Blanchard et al. (2024). The level 2 WebbPSF models were updated since the analysis presented in P. K. Blanchard et al. (2024), so we re-reduce the $\Delta t = 194.74$ days for a consistent data reduction procedure. This results in changes in the photometry <0.17 mag. These measurements are listed in Table 1.

3. Afterglow and Host-galaxy Photometry

3.1. HST

3.1.1. GALFIT Modeling

We use GALFIT (C. Y. Peng et al. 2010) on each of the drizzled images to measure the magnitude of the afterglow and determine a host-galaxy model. We start by constructing a point-spread function (PSF) for each of our images. We use a custom routine utilizing the astropy package EPSFBuilder (L. Bradley et al. 2023) and Source Extractor (E. Bertin & S. Arnouts 1996) to construct a PSF model for each image. We use approximately 40 stars to construct each PSF, with each star being hand-selected to avoid stars with close companions or contamination from diffraction spikes (Figure 1). We attempted to use the same stars in each image, however different positional angles across visits changed the

orientation of the diffraction spikes and the total field of view in each image. We use Source Extractor to determine the centroid of each star to ensure the cutouts used by EPSFBuilder are well centered. In visual examinations of the output PSF, we find the best choices for the oversampling and maxiters parameters are 1 and 10, respectively, across all images.

The field around our afterglow and host galaxy is well populated with stars. There are several stellar sources nearby that have bright diffraction spikes contaminating our source (see Figure 1). These stars also contribute scattered light that complicates making robust measurements of the background, and hence of the afterglow and host galaxy. For our F110W and F160W imaging, we opt to use a fitting region for GALFIT that includes four additional sources to the southeast of the host galaxy. This allows us to maximize the number of background pixels available to GALFIT while excluding bright, saturated sources that GALFIT would be unable to model well. Our results are not sensitive to the details of the crop region, as the final region was selected by minimizing the change in recovered afterglow magnitudes, assuming a constant galaxy model. For our F814W imaging, since the plate scale ($0.^{\circ}02 = 1$ pix) is much smaller than that of our WFC3 IR imaging ($0.^{\circ}065 = 1$ pix), we use a different fitting region that does not include any additional sources. We hold each respective fitting region constant across all visits to standardize our photometry.

We assume a Sérsic profile as the model of the galaxy in one visit and hold it constant across other visits. The brightness

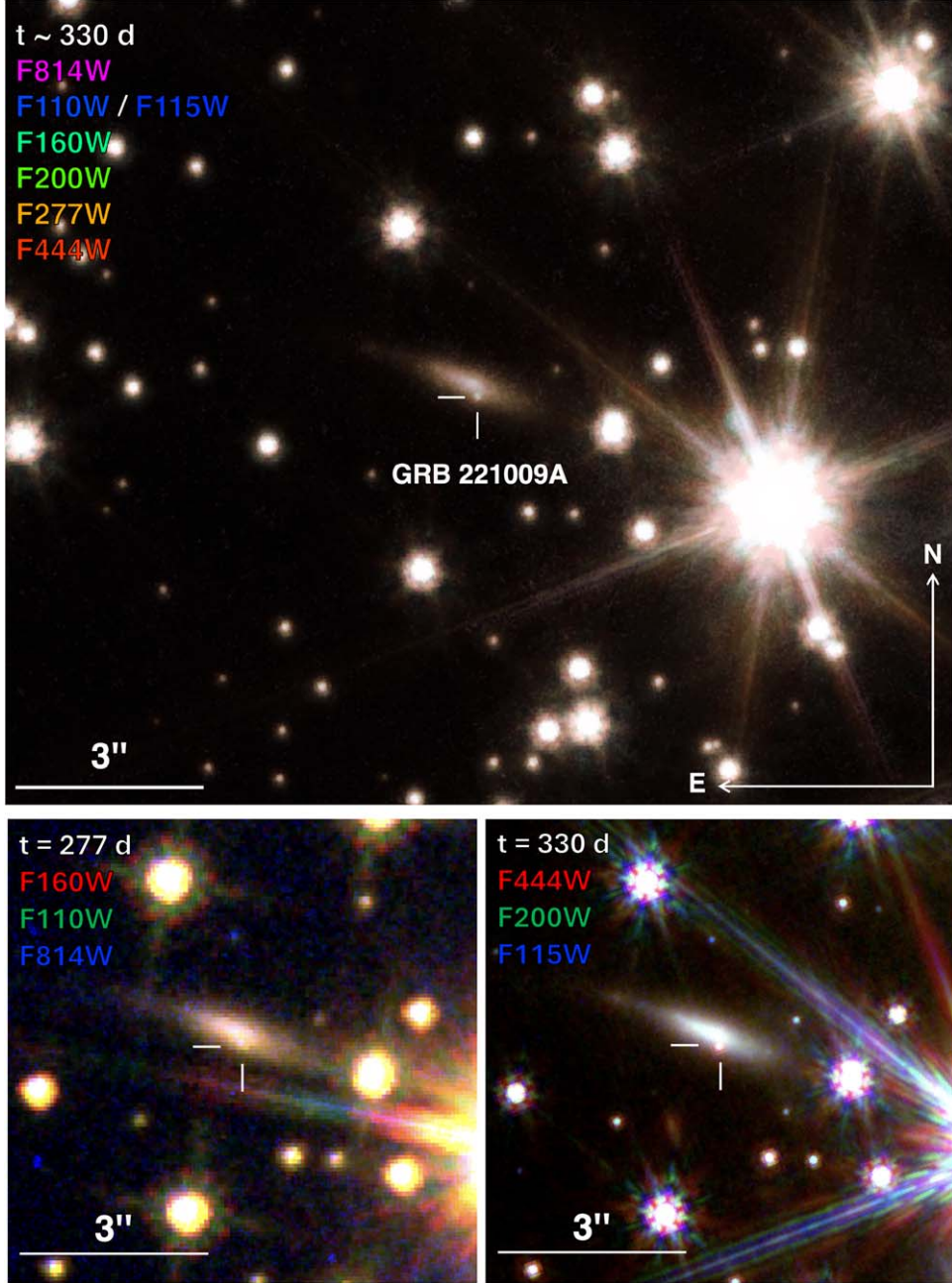


Figure 1. Top: a $15''$ HST/JWST V3 ($t \sim 330$ days) composite image centered at the afterglow. The position is marked with white crosshairs. In all panels, the date of imaging, color, and filter are listed in the top-left corner. North is up, and east is to the left. Lower left: a V2 HST composite image. The afterglow is blended with the host galaxy and there are several diffraction spikes nearby. Lower right: a V3 JWST composite image. The afterglow is clearly detected.

contrast between the underlying host galaxy and afterglow is largest in the V1 imaging, so to best separate contributions from the two sources, we use V1 imaging to measure the F110W and F160W galaxy models. To measure the F814W host-galaxy model, we use V3 imaging, since we do not have V1 imaging and there is a diffraction spike going through the galaxy in V2. The best-fitting parameters for the galaxy profiles are listed in Table 2.

With these galaxy profiles, fitting regions, and PSFs, we use GALFIT to measure the magnitude of the afterglow. We allow the sky to be a free “tilted plane” model (i.e., dy and dx are free parameters within GALFIT). For the F110W and F160W imaging, the afterglow and galaxy model are determined simultaneously in the V1 imaging, and for F814W, in the V3 imaging. The residual images were visually inspected for each

Table 2
GALFIT Host-galaxy Best-fitting Parameters

Parameter	F110W	F160W	F814W
m (mag)	21.92 ± 0.02	21.29 ± 0.02	23.14 ± 0.02
R_e (arcsec)	0.70 ± 0.02	0.69 ± 0.02	0.71 ± 0.02
n	1.21 ± 0.05	1.16 ± 0.04	1.04 ± 0.03
b/a	0.23 ± 0.00	0.23 ± 0.00	0.28 ± 0.00
θ (deg)	67.39 ± 0.42	67.12 ± 0.40	68.66 ± 0.37

Note. m is the magnitude, R_e the half-light radius, n the Sérsic index, b/a the axis ratio, and θ the orientation angle. GALFIT reports all measurements to two decimals, so the 0.00 uncertainty on the axis ratio (for all filters) represents an uncertainty measured <0.005 . The F110W and F160W Sérsic models were fit to the V1 images. The F814W model was fit to the V3 image.

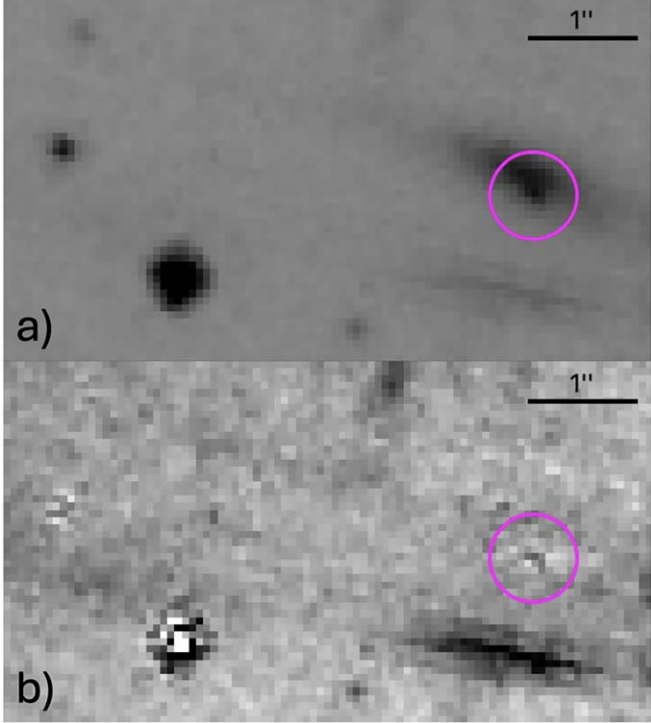


Figure 2. (a) A crop of the V1 F160W image. The magenta region has a radius of 0.4 and is centered at the location of the afterglow. Black shows positive flux. (b) The GALFIT residual of the image above. The scale and stretch have been modified to see fine structure. There is a slight undersubtraction of the afterglow. North is up, and east is to the left.

reported model. The GALFIT-derived magnitudes and their statistical uncertainties are listed in Table 1. A. J. Levan et al. (2023) also fit a Sérsic model to the host galaxy. They find $m_{\text{F160W}} = 20.92 \pm 0.10$ mag, which is slightly brighter than our measurement of $m_{\text{F160W}} = 21.29 \pm 0.02$ mag, but within 3σ agreement. They also find $n_{\text{F160W}} = 1.71 \pm 0.18$ and $b/a_{\text{F160W}} = 0.22 \pm 0.01$. Our axis ratios are in agreement, however our Sérsic index of 1.16 ± 0.04 is smaller, though in 3σ agreement. The afterglow is brighter by ~ 4 mag at the time of the observations in A. J. Levan et al. (2023), which could explain the differences in our galaxy models.

3.2. Difference Imaging

To confirm the reliability of GALFIT to decompose the blended point source and host (see Figure 2 for an example), we perform photometry on subtracted images to measure the brightness difference of the afterglow. We use HOTPANTS (A. Becker 2015) to create these subtraction images. We have successful subtraction in the V1–V3 F160W and the V2–V3 F814W imaging, which allows us to perform photometry. In the rest, we are unable to adequately perform photometry due to scattered light.

We show the usable F160W and F814W difference images in Figure 3. We clearly detect a source in the F160W difference image. We use PhotUtils PSF photometry (L. Bradley et al. 2023) to measure a difference flux for this source. Using the GALFIT V3 magnitude as an anchor, we measure a V1 F160W afterglow magnitude of 24.37 ± 0.07 mag. This is consistent at the 3σ level with the GALFIT V1 F160W magnitude of 24.67 ± 0.13 mag. As shown in Figure 2, there is a slight undersubtraction of the afterglow

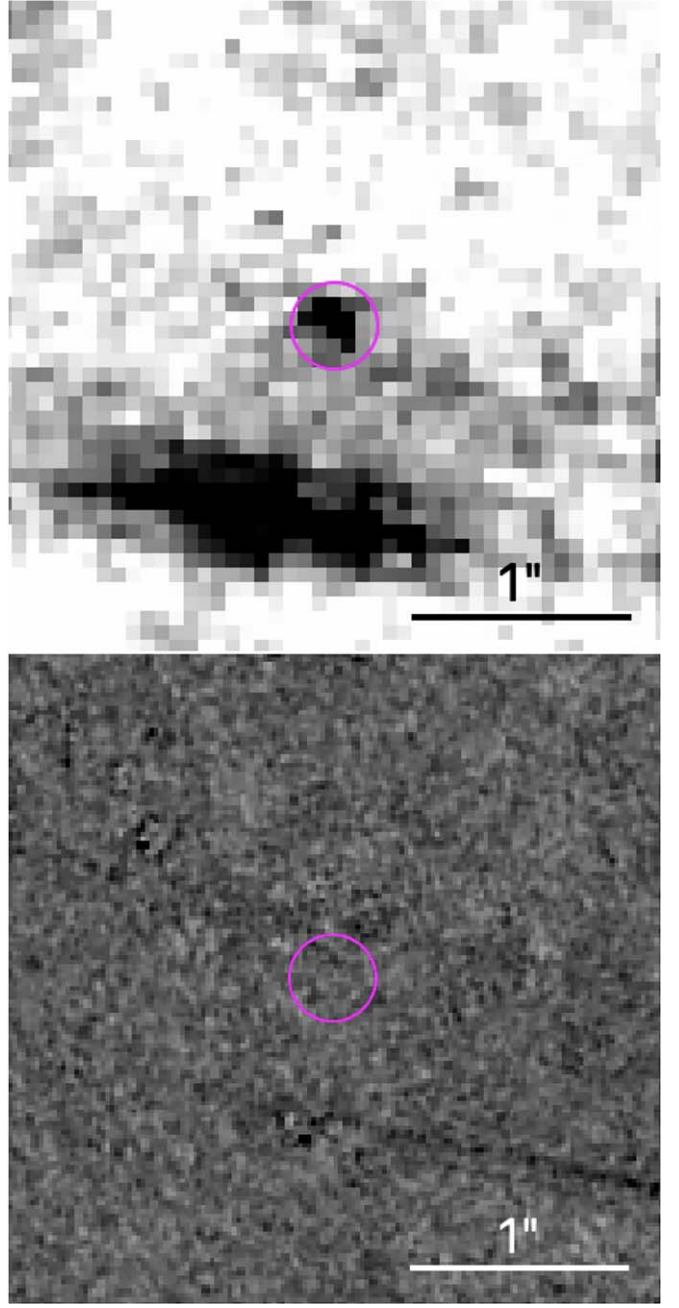


Figure 3. Top: a 3'' cutout of the subtraction image between V3 and V1 F160W. The afterglow is clearly detected in the center of the image. There is an unsubtracted diffraction spike at the bottom center. Bottom: a 3'' cutout of the subtraction image between V3 and V2 F814W. There is no source detected, indicating minimal fading between the two epochs. North is up, and east is to the left. In both panels the magenta region has a 0.2 radius and is centered at the location of the afterglow.

in the GALFIT residual. For this reason, we defer to the HOTPANTS magnitude for our analysis of the V1 F160W photometry, though we find that our results are not sensitive to this choice (see Section 4.3). Furthermore, we use the “HP” or “GF” shorthand to designate if we use the HOTPANTS or GALFIT measurement, respectively. There is no source visible at the location of the afterglow in the F814W residual image, and we confirm a nondetection to a 3σ confidence limit using aperture photometry.

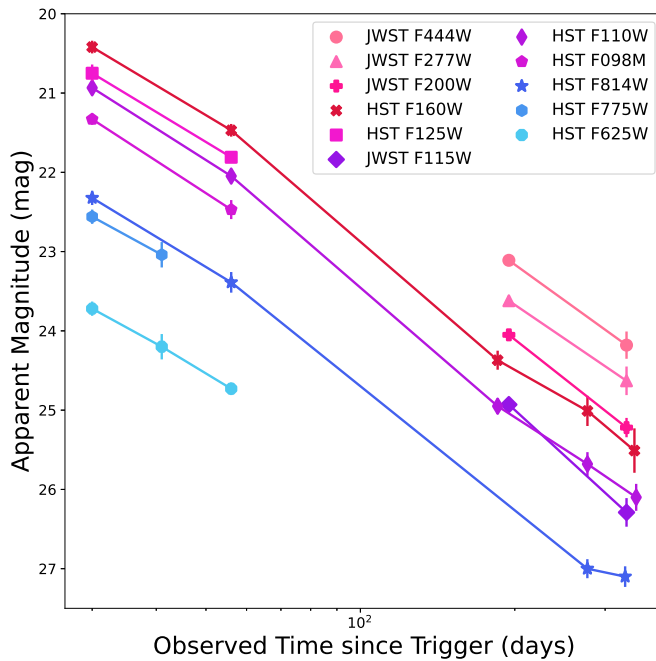


Figure 4. Observed HST and JWST light curve of GRB 221009A. The lines connecting the data are meant to guide the eye. The F160W measurement at $t = 185$ days (V1) is from our difference imaging. Early HST data ($t < 60$ days) in all filters except F110W and F814W are from A. J. Levan et al. (2023). Early F110W and F814W data and their uncertainties were interpolated from the other filters. Uncertainties are sometimes smaller than the marker.

3.3. Systematic Uncertainty Estimation

GALFIT is known to underestimate the uncertainty in all parameters (C. Y. Peng et al. 2010). We therefore consider the reported uncertainty as a “partial” uncertainty of the measurement. To estimate the systematic uncertainty, we perform a custom source injection routine using GALFIT to recover the magnitude. We inject ~ 600 point sources along an ellipse at the distance of the afterglow from the host centroid with the same b/a and position angle as the Sérsic profile (see Table 2). We do not inject sources within 1 PSF FWHM of the center of the afterglow. When using GALFIT to recover the brightness of the injected sources, we use the same image crop as was used to measure the afterglow. We ensure that the magnitude of the injected source is the only free parameter of the injected source point-source model. We apply an offset to the injected source magnitude until the median of the recovered magnitudes is within 0.01 mag of what was measured for the afterglow. We report the 1σ measurement of this recovered-source magnitude histogram as the systematic uncertainty. For the JWST data, we assume 0.05 mag systematic uncertainty on the $t = 194.74$ days data and 0.10 mag systematic uncertainty on the $t = 330.26$ days data, based on experience reducing other Level 3 JWST imaging (P. K. Blanchard et al. 2024). Measurements of the systematic uncertainty are listed in Table 1.

4. Discussion

4.1. HST and JWST Light Curves

We present light curves of the HST and JWST observations in Figure 4. We supplement our late-time HST observations with early HST photometry published in A. J. Levan et al. (2023). We cubic-spline interpolate their observations in F125W, F098M, F775W, and F625W at $t = 30$, and again at

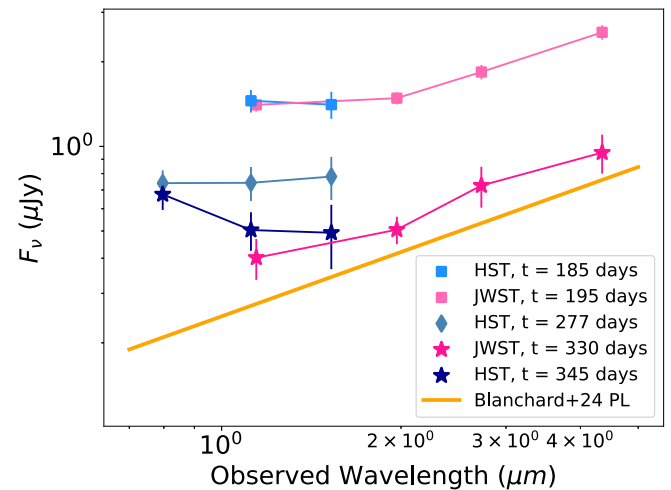


Figure 5. Late-time dust-corrected HST and JWST SED of GRB 221009A. As in Figure 4, the lines connecting the data are meant to guide the eye. We use the HOTPANTS measurement for V1 F160W. The data have been extinction-corrected assuming the F99 dust model ($A_V = 4.63$ mag, $R_V = 4.24$). The JWST photometry at $t = 195$ days and the best-fit power-law model for the afterglow spectrum (orange) are from P. K. Blanchard et al. (2024) with $F_\nu \propto \nu^{-0.76}$. V1 is shown with squares, V2 with diamonds, and V3 with stars. The power-law spectrum has been arbitrarily scaled. There is a clear disagreement between the power-law model and the afterglow photometry at wavelengths bluerward of $2 \mu\text{m}$ at $t \sim 330$ days.

56 days post-trigger to F110W and F814W for better comparison to our observations. One immediate observation is the flattening of the F814W light curve at $t > 277$ days. We present detailed light-curve modeling and interpretation in Section 4.3.

4.2. Spectral Energy Distribution

We consider two dust correction models for the data. The first law is that from E. L. Fitzpatrick (1999, “F99”), while the second is from K. D. Gordon et al. (2023, “G23”), which is better calibrated for data in our observed JWST bands. For these laws and for this source, P. K. Blanchard et al. (2024) find $A_V = 4.63$ mag, $R_V = 4.24$ (F99), and $A_V = 4.37$ mag, $R_V = 3.07$ (G23). We note that these A_V measurements represent the *total* extinction along the line of sight. We discuss in Section 4.4 the effect of this choice on our results, though we find that our results are not statistically sensitive to this choice. For consistency with the analysis in P. K. Blanchard et al. (2024), we assume the F99 dust correction as the fiducial, and unless otherwise explicitly stated it should be assumed the F99 dust correction was used.

We present the SED (HST/F814W – JWST/F444W) at each epoch in Figure 5. We have near-contemporaneous HST and JWST observations at $t \sim 190$ days and at $t \sim 330$ days, and we find good agreement between the two data sets based on the smooth SED shape across HST/F110W – JWST/F200W. We include in Figure 5 the best-fit spectral power law ($F_\nu \propto \nu^{-0.76}$) for the afterglow from P. K. Blanchard et al. (2024). This power law shows agreement with both JWST data sets redward of $2 \mu\text{m}$, but we see evidence for a strong blue component. The disagreement from the afterglow power law is strongest in F814W, but is evident in all HST filters at $t \sim 330$ days. At $t \sim 330$ days, we do not expect this source to be exclusively explained by a SN, similar to other GRB-associated SNe (A. Clocchiatti et al. 2011). To test this expectation, we attach a $F_\lambda \propto \lambda^{-4}$ blackbody tail to the *BVRI* measurements of

SN 1998bw from A. Clocchiatti et al. (2011). We then K -correct the SN 1998bw f_λ to the distance of GRB 221009A and calculate f_ν at $t = 330$ days (observer frame) in the HST and JWST filters. The $t = 330$ day SN spectrum peaks in F814W at $0.2 \mu\text{Jy}$, decreasing as λ^{-4} with increasing wavelength. To explain the blue component, the SN associated with GRB 221009A would need to be a factor of ~ 3 times brighter than SN 1998bw—strongly inconsistent with early results finding an upper limit of $\sim 0.7 \times$ SN 1998bw (G. P. Srinivasaragavan et al. 2023). A natural explanation for the blue excess is that in addition to the fading afterglow and SN, there is some additional source—perhaps a star cluster or a light echo—underlying the GRB that is not accounted for in our host subtraction. We explore these scenarios in Section 4.4.

4.3. Light-curve Modeling

We fit three afterglow decay models to our data:

1. A single power law plus SN:

$$f_\nu(t) = t^{-\alpha_1} + S_{\text{SN}} \times F_{\text{SN 1998bw}}. \quad (1)$$

2. A broken power law plus SN:

$$f_\nu(t) = 2^{1/s} \times F_{t_{\text{brk}}} \times \left(\left(\frac{t}{t_{\text{brk}}} \right)^{\alpha_1 s} + \left(\frac{t}{t_{\text{brk}}} \right)^{\alpha_2 s} \right)^{-1/s} + S_{\text{SN}} \times F_{\text{SN 1998bw}}. \quad (2)$$

3. A broken power law plus SN plus constant source:

$$f_\nu(t) = 2^{1/s} \times F_{t_{\text{brk}}} \times \left(\left(\frac{t}{t_{\text{brk}}} \right)^{\alpha_1 s} + \left(\frac{t}{t_{\text{brk}}} \right)^{\alpha_2 s} \right)^{-1/s} + S_{\text{SN}} \times F_{\text{SN 1998bw}} + F_c. \quad (3)$$

Where t is the time in days, S_{SN} is the flux scaling of SN 1998bw, $F_{\text{SN 1998bw}}$ is the flux of SN 1998bw, t_{brk} is the break time in days, $F_{t_{\text{brk}}}$ is the flux at time $t = t_{\text{brk}}$, α_1 is the pre-break (or only) slope, α_2 is the post-break slope, s is the smoothing parameter, and F_c is the flux of the constant source. While we are unable to fit for the smoothing parameter with our data set, because the physical processes governing the two slopes is the same, we expect a relatively smooth transition. We elect to use $s = 3$, however our results are not significantly sensitive to this choice.

For the SN component, we assume a SN 1998bw light curve with allowance for time stretching. We start with the host extinction-corrected *BVRI* (rest-frame) data from A. Clocchiatti et al. (2011) and attach a $f_\lambda \propto \lambda^{-4}$ blackbody tail redward to estimate f_λ . We then K -correct the SN 1998bw f_λ to the distance of GRB 221009A and calculate light curves in each of the filters of interest.

We fit the single power law plus scaled SN (“SPL + SN”) to the early data ($t = 1$ –56 days, *riz*, *rizy_{PS}*, and HST; M. Shrestha et al. 2023; M. D. Fulton et al. 2023; A. J. Levan et al. 2023, respectively) using a Markov Chain Monte Carlo (MCMC) sampler with *emcee* (D. Foreman-Mackey et al. 2013) and extrapolate to later times. We fit for the magnitude at $\Delta t = 10$ days in F110W and apply $f_\nu \propto \nu^{-0.76}$ (P. K. Blanchard et al. 2024) to calculate the magnitude in other filters. We assume the same α_1 for all filters. We run 32 walkers for 5000 steps and discard the first 500 steps as burn-in. We use uniform priors on

α from 1.0 to 3.5, $m_{\text{fit,F110W}}$ from 10 to 40 mag, t_{stretch} of 0.5 to 3.0, and S_{SN} of 0 to 10. Shown in the top-left panel of Figure 6, the extrapolation of the power-law model is a poor fit to the later ($t > 185$ days) data. We report the results of our fitting in Table 3.

We repeat our MCMC *emcee* fitting now assuming single power laws for the *riz*, *rizy_{PS}*, and JWST data and a broken power law for the full HST data with the addition of a SN in all filters. We refer to this model as “BPL + SN.” The choice to use single power laws for the ground and JWST data is because they do not cover the break window and therefore are not able to probe t_{brk} or the opposing slope. We again fit for the magnitude at t_{brk} in F110W and apply $f_\nu \propto \nu^{-0.76}$ to calculate the magnitude in other filters. We assume the same α_1 and α_2 for all filters. We assume uniform priors on α_1 of 1.0–2.0, α_2 of 2.0–5.0, $\log(t_{\text{brk}})$ of 1.00–2.27 log(days), $m_{t_{\text{brk}},\text{F110W}}$ of 20–30 mag, and again t_{stretch} of 0.5 to 3.0 and S_{SN} of 0–10. We assume α_1 for the slopes of the *riz* and *rizy_{PS}* power laws and α_2 for the slopes of the JWST power laws. We show our fits to the HST and JWST data in the top-right panel of Figure 6. This model is noticeably better than the extrapolation of the single power law, however there is consistent underprediction of the entire F814W data set and most of the late-time F110W data. We report the results of our fitting in Table 3.

The next fit to the data is the addition of a constant source to the broken power law plus SN model described above (“BPL + SN + C”). This choice is motivated by the underpredictions from the broken power law plus SN modeling and the deviation in the SED from the assumed spectral power law ($f_\nu \propto \nu^{-0.76}$) from P. K. Blanchard et al. (2024), as shown in Figure 5. We again calibrate to the F110W data set assuming $f_\nu \propto \nu^{-0.76}$ and assume the same α_1 and α_2 for all filters. We assume the same uniform priors as before. We fit for the constant source magnitude in each HST filter and JWST F115W, with a prior on each m_c of 24–29 mag. We assume the same constant for F110W and F115W due to their near-equivalent effective wavelengths and to reduce the total number of parameters. We are not able to probe the contribution of a late-emerging constant with the early ground data, and the V3 SED shows no evidence for an additional component in F200W, F277W, and F444W, so we set the constant in these filters to have zero flux. We show our fits in Figure 6, and we report the results of our fitting in Table 3.

The final fit to the data is a broken power law plus constant with no consideration of a SN contribution (“BPL + C”). While this is an unphysical model, given the spectroscopic detection in P. K. Blanchard et al. (2024), this can be used to test the sensitivity of our model to the inclusion of a SN component. We repeat the same priors as before, and we assume the HOTPANTS measurement of V1 F160W. We also repeat the same assumptions about which filters have a constant with zero flux. We report the results of our fitting in Table 3.

We perform χ^2 tests for these data and models. We set an uncertainty floor of 0.10 mag. For the best-fit SPL + SN model, we measure a χ^2 of 267 with 124 degrees of freedom (d.o.f.). For the best-fit BPL + SN model, we measure a statistic of 249 with 129 d.o.f. For the best-fit BPL + SN + C model, we measure a statistic of 211 with 126 d.o.f. For the best-fit BPL + C model, we measure a statistic of 217 with 128 d.o.f. The SPL + SN model is only compared to the ground and HST data, whereas the other models are also compared to the JWST data, so has a slightly differently defined number of

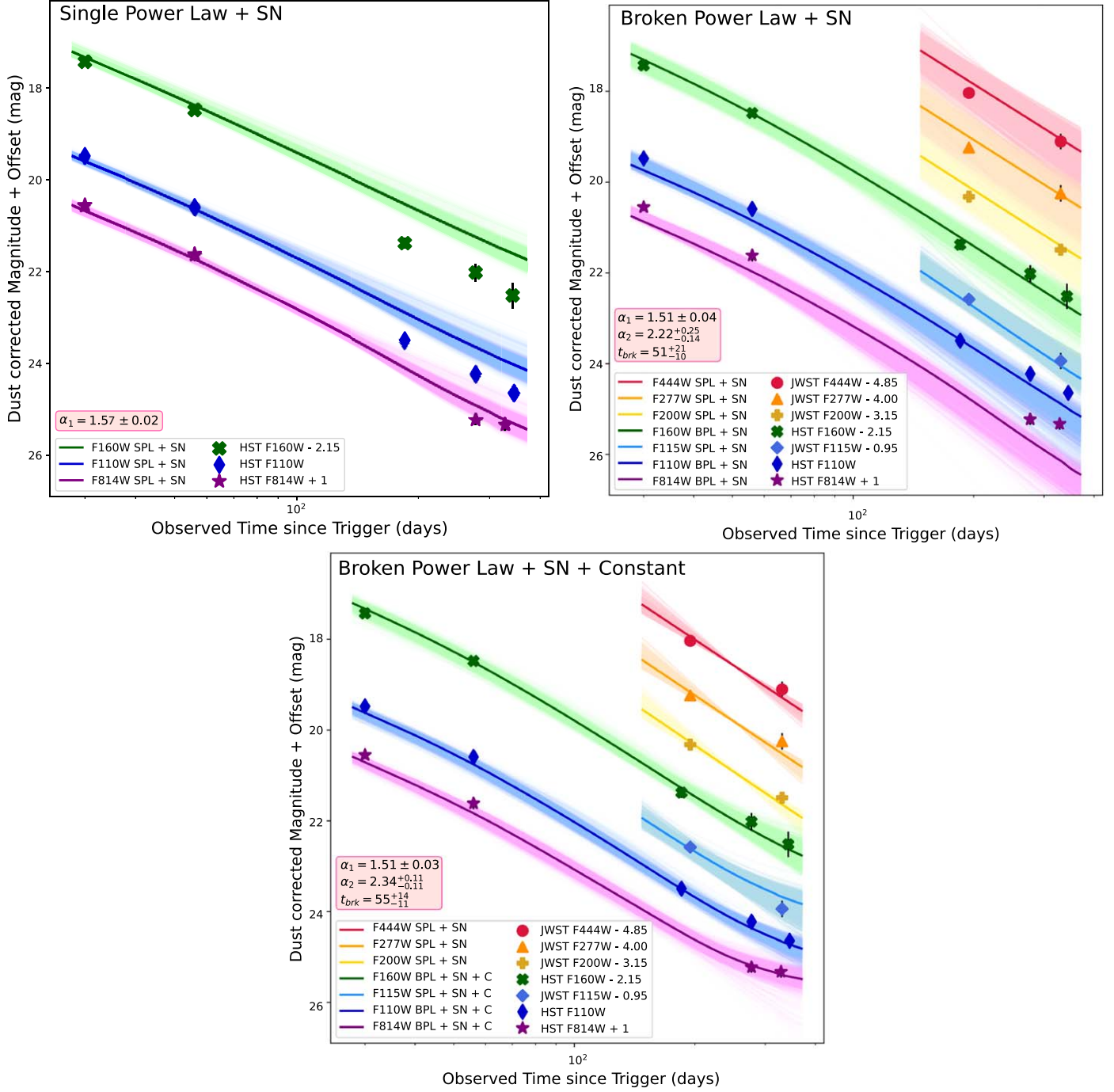


Figure 6. Top left: single power-law fits to early-time data from M. Shrestha et al. (2023), M. D. Fulton et al. (2023), and A. J. Levan et al. (2023) extended to late times; 3060 (68% of 4500) random pulls from each posterior are shown as the lighter shaded lines to show the 1σ uncertainty of the fit. HST observations from A. J. Levan et al. (2023) and those published here are shown as the points with error bars. These observations have been dust-corrected assuming the F99 dust law ($A_V = 4.63$ mag, $R_V = 4.23$) and have been artificially offset. We use the HOTPANTS measurement for V1 F160W. These observations and choices are consistent across all panels. There is clear disagreement between the single power law + SN model extrapolations and the late-time observations in all filters, F160W especially. Top right: the models fit to the data are now a broken power law + SN, and the JWST data have been added. Bottom: the models fit to the data are now a broken power law + SN + constant. The fitting procedures for all panels are described in Section 4.3, and all fitting parameters are listed in Table 3. Uncertainty bars are sometimes smaller than the symbols.

degrees of freedom. From the BPL + SN to BPL + SN + C, we see a decrease in the χ^2 of 38 with a decrease of only 3 d.o.f. Conversely, the χ^2 change from the BPL + SN + C to the BPL + C is an increase of 7 with a decrease of 2 d.o.f. This implies that the constant is strongly preferred while the SN component is weakly preferred.

There is some disagreement on the use of reduced χ^2 tests when assuming nonlinear models (e.g., R. Andrae et al. 2010),

and so we additionally calculate an Akaike information criterion (AIC; H. Akaike 1974) and Bayesian information criterion (BIC; G. Schwarz 1978) for each afterglow model. As shown in Table 4, we are able to statistically rule out both the SPL + SN extrapolations and BPL + SN models with ΔAIC , $\Delta\text{BIC} > 10$ (A. E. Raftery 1995; K. P. Burnham & D. R. Anderson 2004). We also find that our results are not sensitive to our choice of the V1 F160W measurement. We

Table 3
emcee Results Following the Procedure Detailed in Section 4.3

SN Scale (S_{SN})	t_{stretch}	t_{brk} (log days)	α_1	α_2	m_{norm} (mag)	C_{F160W} (mag)	C_{F110W} (mag)	C_{F814W} (mag)
SPL + SN								
F99 HP: $1.96_{-0.38}^{+0.37}$	$0.52_{-0.02}^{+0.04}$...	$1.57_{-0.02}^{+0.02}$...	$17.98_{-0.04}^{+0.04}$
G23 HP: $0.71_{-0.34}^{+0.31}$	$0.57_{-0.06}^{+0.28}$...	$1.49_{-0.02}^{+0.02}$...	$18.04_{-0.04}^{+0.04}$
BPL + SN								
F99 HP: $1.13_{-0.83}^{+0.54}$	$0.56_{-0.06}^{+0.99}$	$1.71_{-0.09}^{+0.15}$	$1.51_{-0.04}^{+0.04}$	$2.22_{-0.13}^{+0.25}$	$20.81_{-0.42}^{+0.73}$
F99 GF: $1.18_{-0.80}^{+0.60}$	$0.56_{-0.05}^{+0.80}$	$1.70_{-0.08}^{+0.15}$	$1.52_{-0.04}^{+0.05}$	$2.21_{-0.12}^{+0.31}$	$20.80_{-0.40}^{+0.70}$
G23 HP: $0.16_{-0.06}^{+0.11}$	$1.99_{-0.53}^{+0.60}$	$1.70_{-0.06}^{+0.07}$	$1.44_{-0.02}^{+0.02}$	$2.41_{-0.12}^{+0.14}$	$20.72_{-0.26}^{+0.30}$
G23 GF: $0.15_{-0.07}^{+0.15}$	$1.98_{-1.07}^{+0.67}$	$1.68_{-0.07}^{+0.08}$	$1.44_{-0.02}^{+0.02}$	$2.43_{-0.19}^{+0.20}$	$20.65_{-0.26}^{+0.34}$
BPL + SN + C								
F99 HP: $1.47_{-0.36}^{+0.39}$	$0.55_{-0.04}^{+0.06}$	$1.74_{-0.11}^{+0.11}$	$1.51_{-0.03}^{+0.03}$	$2.34_{-0.11}^{+0.11}$	$21.00_{-0.49}^{+0.52}$	$25.54_{-0.24}^{+0.35}$	$24.84_{-0.18}^{+0.24}$	$26.13_{-0.65}^{+1.22}$
F99 GF: $1.30_{-0.70}^{+0.44}$	$0.57_{-0.06}^{+0.21}$	$1.64_{-0.16}^{+0.11}$	$1.50_{-0.04}^{+0.04}$	$2.28_{-0.15}^{+0.15}$	$20.56_{-0.70}^{+0.54}$	$25.60_{-0.27}^{+0.55}$	$24.87_{-0.27}^{+0.41}$	$26.43_{-0.85}^{+1.40}$
G23 HP: $0.36_{-0.24}^{+0.33}$	$0.71_{-0.17}^{+0.54}$	$1.75_{-0.08}^{+0.07}$	$1.45_{-0.02}^{+0.02}$	$2.45_{-0.10}^{+0.10}$	$20.95_{-0.38}^{+0.33}$	$25.59_{-0.24}^{+0.44}$	$25.22_{-0.23}^{+0.32}$	$25.97_{-0.60}^{+1.27}$
G23 GF: $0.29_{-0.19}^{+0.34}$	$0.74_{-0.23}^{+0.77}$	$1.72_{-0.12}^{+0.10}$	$1.45_{-0.02}^{+0.03}$	$2.41_{-0.15}^{+0.17}$	$20.82_{-0.50}^{+0.46}$	$25.72_{-0.34}^{+0.61}$	$25.34_{-0.32}^{+0.45}$	$26.40_{-0.90}^{+1.44}$
BPL + C								
F99 HP:	$1.61_{-0.09}^{+0.09}$	$1.43_{-0.02}^{+0.02}$	$2.35_{-0.09}^{+0.10}$	$20.12_{-0.38}^{+0.36}$	$25.48_{-0.31}^{+0.55}$	$24.84_{-0.26}^{+0.31}$	$26.63_{-1.00}^{+1.43}$
G23 HP:	$1.73_{-0.07}^{+0.07}$	$1.42_{-0.02}^{+0.02}$	$2.43_{-0.09}^{+0.09}$	$20.73_{-0.27}^{+0.27}$	$25.56_{-0.27}^{+0.43}$	$25.19_{-0.23}^{+0.27}$	$26.32_{-0.74}^{+1.29}$

Note. The normalization magnitude for the single power law (SPL) + SN is m_{F110W} at time $t = 1$ day. The normalization magnitude for the broken power law (BPL) + SN, BPL + SN + Constant (C), and BPL + C is m_{F110W} at time $t = t_{\text{brk}} \log(\text{days})$. The choice of V1 F160W for the BPL models is indicated in the “SN Scale” column. “F99” refers to the choice of dust correction, where we use the E. L. Fitzpatrick (1999) law with $A_V = 4.63$ mag, $R_V = 4.23$. “G23” refers to the choice of the K. D. Gordon et al. (2023) law, with $A_V = 4.37$ mag, $R_V = 3.07$. “HP” (“GF”) is meant to refer to the HOTPANTS (GALFIT) choice of V1 F160W.

proceed in the next section with interpretation of the BPL + SN + C model.

4.4. Model Interpretation

In the broken power law plus SN plus constant model, using the image subtraction measurement for V1 F160W, we find $\alpha_1 = 1.51 \pm 0.03$, $\alpha_2 = 2.34 \pm 0.11$, $t_{\text{brk}} = 10^{1.74 \pm 0.11}$ days, a SN 1998bw flux scaling $S_{SN} = 1.47_{-0.36}^{+0.39}$, a SN 1998bw time stretch factor $t_{\text{stretch}} = 0.57_{-0.04}^{+0.06}$, and dust-corrected constant source magnitudes of $m_{\text{F814W}} = 26.13_{-0.65}^{+1.22}$ mag, $m_{\text{F110W/F115W}} = 24.84_{-0.18}^{+0.24}$ mag, $m_{\text{F160W}} = 25.54_{-0.24}^{+0.35}$ mag. All parameter measurements for all models and choices of V1 F160W are given in Table 3.

4.4.1. Supernova Component

In the preferred model, we find a SN component with a SN 1998bw flux scaling, S_{SN} , in 3σ consistency with the early results (e.g., M. D. Fulton et al. 2023; T. Laskar et al. 2023; A. J. Levan et al. 2023; M. Shrestha et al. 2023; G. P. Srinivasaragavan et al. 2023) and in 2σ consistency with the results from the JWST-focused study (P. K. Blanchard et al. 2024). This is only true, however, due to the large uncertainty on our measurement. We ran a model assuming a BPL + C with no SN, and we find all parameters (except α_1) in $\sim 1\sigma$ agreement with our results from the broken power law plus constant plus SN fit. The “new” $\alpha_1 = 1.43 \pm 0.02$ is instead only in 3σ agreement with the BPL + SN + C measured quantity. In a statistical AIC test, we are able to rule out this model (K. P. Burnham & D. R. Anderson 2004); however, since our $\Delta\text{BIC} < 10$, this model is less preferred

Table 4
Statistical Results for the Considered Transient Models

Model	AIC	ΔAIC	BIC	ΔBIC
HOTPANTS F160W - F99				
SPL + SN	-66	167	-49	149
BPL + SN	-202	31	-176	22
BPL + SN + C	-233	0	-198	0
BPL + C	-219	14	-189	8
GALFIT F160W - F99				
SPL + SN	-38	189	-20	171
BPL + SN	-201	25	-174	17
BPL + SN + C	-226	0	-191	0
HOTPANTS F160W - G23				
SPL + SN	66	321	83	309
BPL + SN	-241	14	-215	11
BPL + SN + C	-255	0	-220	6
BPL + C	-255	0	-226	0
GALFIT F160W - G23				
SPL + SN	97	343	114	325
BPL + SN	-235	11	-209	2
BPL + SN + C	-246	0	-211	0

Note. $\Delta\text{AIC} = \text{AIC}_{\text{model}} - \text{AIC}_{\text{min}}$. ΔBIC is similarly defined. “F99” refers to the choice of dust correction, where we use the E. L. Fitzpatrick (1999) law with $A_V = 4.63$ mag, $R_V = 4.23$. “G23” refers to the choice of the K. D. Gordon et al. (2023) law, with $A_V = 4.37$ mag, $R_V = 3.07$.

(A. E. Raftery 1995) rather than ruled out. In the repeated analysis assuming the G23 dust correction, for the BPL+SN+C model, we find a flux scaling factor of $\sim 0.3 \pm 0.3$, which is in $\sim 3\sigma$ consistency with the early results and the F99 results for the same model; however, this is again only true due to the large uncertainty. Lastly, as mentioned in the previous section, the χ^2 results show a weak preference for the SN component. We therefore consider our result of the SN 1998bw flux scaling of $S_{\text{SN}} = 1.47^{+0.39}_{-0.36}$ as a broad upper limit rather than a strong detection of SN 2022xiw.

4.4.2. Jet Break

We find support for a break at $t_{\text{brk}} = 10^{1.7 \pm 0.1}$ (~ 50) days. This result is robust across all model, data, and dust choices. Considering the numerous jet-break models presented in H. Gao et al. (2013, i.e., “Phase 2” to “Phase 3”), we find only one that is consistent with our data. This model requires slow-cooling electrons in a wind medium, and an electron energy spectral index $p > 2$ (Tables 13/14 and 18/19 of H. Gao et al. 2013). While these slope descriptions do not allow us to fully determine the order of the self-absorption frequency ν_a , cooling frequency ν_c , and characteristic frequency ν_m , (i.e., the pre- and post-break slopes are identical for $\nu_a < \min(\nu_m, \nu_c)$ and $\nu_m < \nu_a < \nu_c$ with these assumptions), in either case $\nu_m < \nu_c$. This model invokes $\alpha_1 = (3p - 1)/4$, $\alpha_2 = (3p + 1)/4$, and $\beta = (p - 1)/2$ (H. Gao et al. 2013). From our assumed spectral index, $\beta = 0.76 \pm 0.07$ (P. K. Blanchard et al. 2024), in this jet-break interpretation we would expect $\alpha_1 = (3\beta + 1)/2 = 1.64 \pm 0.10$ and $\alpha_2 = (3\beta + 2)/2 = 2.14 \pm 0.11$. This provides an expected change in slope of $\Delta\alpha = 0.50 \pm 0.21$. The expected parameters are in $\sim 1\sigma$ agreement with our measured $\alpha_1 = 1.51 \pm 0.03$, $\alpha_2 = 2.34 \pm 0.11$, and $\Delta\alpha = 0.83 \pm 0.14$. We therefore report $p = 2\beta + 1 = 2.52 \pm 0.14$ for this decay model. In the repeated analysis assuming the G23 model, we find a pre-break slope of $\alpha_1 = 1.45 \pm 0.02$ and a post-break slope of $\alpha_2 = 2.45 \pm 0.10$, resulting in $\Delta\alpha = 1.00 \pm 0.12$. These measured parameters are in 3σ consistency with the F99 measured parameters, and they are also in $\sim 1\sigma$ consistency with the predicted jet-break parameters listed prior. We find consistency with T. Laskar et al. (2023), who report $p = 2.53$, $\nu_m < \nu_c$, and predict a jet break at $t \sim 130$ days based on an observed 3 mm flux. The interpretation in A. J. Levan et al. (2023) is incompatible with our interpretation, as they assume an early jet break at $t < 0.03$ days and $p < 2$. In a recent radio-focused analysis of GRB 221009A, L. Rhodes et al. (2024) did not find evidence for a jet break out to 475 days post-burst, however they do note that lateral structure in the jet could have prevented detection.

Assuming Equation (2) from W. Zhao et al. (2020, and references therein), which describes the jet opening angle assuming a wind profile and using $E_{\gamma, \text{iso}} = 10^{55}$ erg (S. Lesage et al. 2023), a gamma-ray efficiency $\eta = 0.2$, and a wind parameter $A^* = 1$, a jet break at ~ 50 days leads to a jet half-opening angle of $\theta_{\text{jet}}(\text{Wind}) = 4^\circ$. This is in contradiction to the earlier claims of a very narrow jet (e.g., ~ 0.8 , 1.5 ; LHAASO Collaboration et al. 2023; M. Negro et al. 2023, respectively). If we instead use a wind parameter $A^* = 10^{-3}$, we calculate $\theta_{\text{jet}}(\text{Wind}) = 0.7^\circ$, which is in better agreement with early results. This implies that the wind environment of GRB 221009A has a much higher velocity or much lower mass-loss rate than the standardly assumed model. Alternatively, B. O’Connor et al. (2023) suggests a two-component jet model, which would allow for two jet breaks.

While we show support for the break at $t \sim 50$ days being interpreted as a jet break, there is also a break in the optical data at ~ 1 day (M. Shrestha et al. 2023). Using the “Wind” assumptions (including $A^* = 1$) and equation above, a jet break at 1 day leads to a jet half-opening angle of $\theta_{\text{jet}}(\text{Wind}) = 1^\circ$. This break at $t \sim 1$ day, however, has also been interpreted as coming from the spectral “cooling” break (T. Laskar et al. 2023). Robust classification of the $t \sim 50$ days optical break, especially in the context of earlier optical breaks, can only be achieved with modeling of the full multiwavelength data set, which we leave for future work (T. Laskar et al. 2025, in preparation).

The jet half-opening angle and isotropic gamma-ray energy can be used to calculate the energy of the jet via $E_\gamma = E_{\gamma, \text{iso}}(1 - \cos(\theta_{\text{jet}}))$ (D. A. Frail et al. 2001). We calculate $E_\gamma = 2.4 \times 10^{52}$ erg. X.-G. Wang et al. (2018) found a mean $\log(E_\gamma / \text{erg}) = 49.54 \pm 1.29$ and a mean jet half-opening angle of $\theta_{\text{jet}} = 2.5 \pm 1^\circ$ in an optical and X-ray study of 99 GRB afterglows. Our measurements are in $\sim 1\sigma$ consistency with the mean values. This implies that while GRB 221009A is extraordinary in observed properties, it is relatively average in intrinsic properties.

4.4.3. Star Cluster or Dwarf Satellite Galaxy

In the JWST NIRSpec and MIRI spectra of the host galaxy at the location of the GRB, strong ionized hydrogen emission (H II) and strong molecular hydrogen emission (H_2) were detected (P. K. Blanchard et al. 2024). H II regions are ionized by the UV radiation from recently formed massive stars. Strong H II emission is a sign of strong UV radiation, which could originate from many stars, i.e., a star cluster. Molecular hydrogen is also known to be associated with recent star formation (e.g., A. Verma et al. 2024). The association of GRB 221009A with a star cluster would be the first such detection, but it would not be in conflict with theoretical expectations from massive stellar collapse. GRB host galaxies at $z < 1.2$ have been found to be bluer (i.e., UV brighter) than core-collapse SN host galaxies, with the increased UV light thought to be caused by recent, intense star formation (K. M. Svensson et al. 2010), and GRBs at $z < 1.2$ are found to occur on the brightest parts of their host galaxy (A. S. Fruchter et al. 2006; K. M. Svensson et al. 2010; P. K. Blanchard et al. 2016; J. D. Lyman et al. 2017). In the context of host-galaxy light distributions, the existence of a GRB within a star cluster (or otherwise dense, star-forming region) is, arguably, expected.

To model a young star cluster at the distance of GRB 221009A, we use the Flexible Stellar Population Synthesis (or FSFS; C. Conroy et al. 2009, 2010; C. Conroy & J. E. Gunn 2010) code with the assumptions of a gas-phase metallicity $Z = 0.12 Z_\odot$ and apparent magnitude $m_{\text{F110W}} = 24.84$ mag at $z = 0.151$ with $A_V = 4.6$ mag across the age range 1–4 Myr. This matches the gas-phase metallicity determined at the location of the GRB (P. K. Blanchard et al. 2024), and we normalize in the F110W band (as opposed to F160W or F814W), as it is our best-measured quantity. We select this age range to force the star cluster to be sufficiently young to still have significant molecular hydrogen (K. Hollyhead et al. 2015). Under these assumptions, if the additional source is interpreted as a star cluster, it would have a mass of $M_* \sim 3 \times 10^5 M_\odot$. Star cluster masses have been well measured for clusters in the SMC, a similarly low metallicity and low star

formation rate (SFR) galaxy, and for this age range there is not a single cluster with a mass $>10^4 M_{\odot}$ (see Figure 8 in D. A. Hunter et al. 2003). A cluster of this mass and age in a low-SFR ($0.17 M_{\odot} \text{ yr}^{-1}$; P. K. Blanchard et al. 2024) galaxy is therefore unexpected.

We do not resolve the source in F814W, and we therefore calculate an upper limit on its radius of 140 pc. A study of 164 star-forming dwarf galaxies at $z = 0.13$ –0.88 found a range of effective radii $r_e = 0.1$ –6 kpc (median $r_e = 1.2 \pm 2.3$ kpc) in the HST-ACS F814W bandpass (A. Calabro et al. 2017). While a dwarf galaxy smaller than our limit of 140 pc is consistent with this distribution, it would have to be one of the smallest ever discovered. Star clusters have linear diameters ~ 20 pc (S. van den Bergh 2006), and are therefore consistent with our limit. Confirmation of this blue source as a star cluster, or otherwise dense star-forming region, can only come from continued blue flux detection after the afterglow and SN have completely faded.

4.4.4. Scattered-light Echo

A scattered-light echo occurs when light from a SN or other bright transient reflects off dust in the host galaxy of the transient. The echo will have an optical light curve as a fading source with a change in decay rate at 2 times the light-travel time of the distance of the scattering dust. The change in slope is dependent on the distance of the scattering dust, the strength of the dust wind, and the presence of forward scattering (R. A. Chevalier 1986). The echo will appear in the spectrum with a SED shape nearly identical to the initially radiated light but with a f_{λ} scaling law of $\lambda^{-\alpha}$, where α ranges from 1 to 2 (R. A. Chevalier 1986; A. A. Miller et al. 2010). It is expected that the SED of the echo is bluer than the transient. Scattered-light echoes have been detected for a number of SNe, including the well-studied and close core-collapse SN 1987A (A. P. S. Crotts et al. 1995; A. Cikota et al. 2023), a close and class-defining SNe Ia, SN 1991T (B. P. Schmidt et al. 1994), one of the most luminous core-collapse SNe, SN 2006gy (N. Smith et al. 2008; A. A. Miller et al. 2010), and one of the closest normal Type Ia SNe, SN 2014J (A. P. S. Crotts 2015; Y. Yang et al. 2018).

A shallowing of the optical light curve from the afterglow decay, as we find tentative support for, is consistent with a scattered-light echo. We also see the SED becoming bluer with time. Our HST and JWST data mostly probe the near-IR (NIR), however the extinction-corrected V3

F814W–F110W color is -0.31 ± 0.21 mag. This converts to a spectral slope $\beta = 0.84 \pm 0.56$. The optical light at early times was dominated by the afterglow, with a spectral shape of $f_{\nu} \propto \nu^{-0.76 \pm 0.10}$ (P. K. Blanchard et al. 2024). The light echo spectral shape should therefore be $f_{\nu} \propto \nu^{1.24}$ assuming $f_{\lambda} \propto \lambda^{-2} \times f_{\lambda, \text{AG}}$, or $f_{\nu} \propto \nu^{0.24}$ assuming $f_{\lambda} \propto \lambda^{-1} \times f_{\lambda, \text{AG}}$. These scalings produce expected F814W–F110W colors of -0.45 mag and -0.08 mag, respectively, in remarkable agreement with our measured color of -0.31 ± 0.21 mag.

We run an emcee fit of a sum of two power laws (similar to Equation (2), but without the SN component) to our dust-corrected $t \sim 330$ day data to further check the feasibility of this interpretation. This fit is shown in Figure 7. We assume a smoothness parameter, $s = -3$, to invert the break angle from the light-curve modeling. We run two fits: one with the redder power-law slope equal to the Atacama Large Millimeter/submillimeter Array (ALMA)-XRT slope at $\Delta t = 190$ days

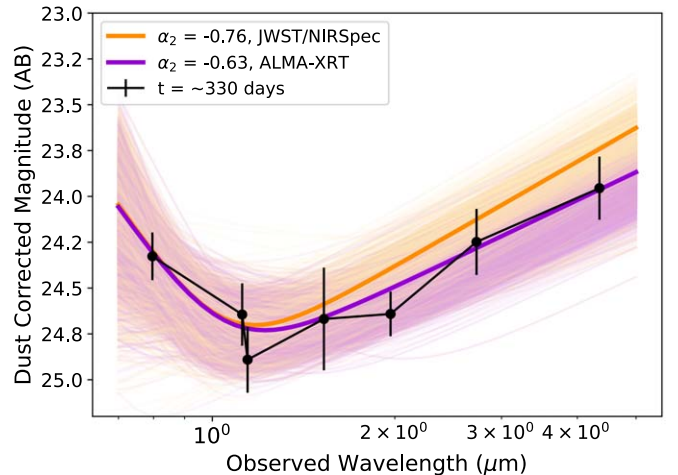


Figure 7. A fit of a sum of two power laws to the $t \sim 330$ day SED. In black is the HST and JWST data as presented in Table 1. In purple and orange are the emcee best fits assuming the ALMA-XRT or JWST/NIRSpec afterglow slopes (P. K. Blanchard et al. 2024) for the red power-law slope, respectively. We also plot 3060 random pulls from the emcee posteriors to show the 1σ uncertainty in the fit. The best-fit blue slopes and their uncertainty are reported in Section 4.4.4.

(observer frame) and the other with a red power-law slope equal to that measured from the JWST/NIRSpec spectrum at $\Delta t = 167$ days, both from P. K. Blanchard et al. (2024). We assume flat priors of 0–4.0 for the blue power-law slope and the two normalization scalings. We measure blue slopes of $1.93_{-0.86}^{+1.15}$ and $1.96_{-0.92}^{+1.10}$, assuming the ALMA-XRT and JWST red slopes, respectively. These slopes convert to expected F814W–F110W colors of $-0.71_{-0.43}^{+0.32}$ mag and $-0.73_{-0.41}^{+0.34}$ mag, both in 1σ consistency with the expected light echo color range of -0.08 to -0.45 mag. If this source continues to have an optical plateau while fading in the NIR bands, this could be confirmation of this blue source as a light echo. If confirmed, this would mark the first detection of an optical light echo from a GRB afterglow.

4.5. Comparison to Other GRBs

GRB 221009A is exceptional in many regards. In the interpretation that the break is a jet break, we compare the jet-break time of $t_{\text{brk}} \sim 50$ days to reported jet-break times of all other GRBs ($N = 138$) through early-2020 reported in W. Zhao et al. (2020). One hundred and thirty of the 138 jet breaks in W. Zhao et al. (2020) are measured from X-ray or optical light curves, while the remaining eight were measured from radio light curves. The median value of their sample of 138 jet-break times is $\log(t_{\text{brk,med}}/s) = 4.78 \sim 0.9$ days, and the standard deviation of their sample is 0.77 dex. The jet-break time of GRB 221009A is later than any object in the sample, though is in 3σ agreement with the median. With that said, the sample of W. Zhao et al. (2020) is observationally biased against GRBs with late ($t > 12$ days) jet breaks, as most GRB afterglows are not observed in the X-ray or optical past 12 days (A. Melandri et al. 2014). Indeed, only five of the 138 GRBs in the sample have jet-break times later than 12 days. The detection of a jet break at a superlatively late time in comparison to this sample is rather an observational consequence of the intrinsic brightness and closeness of the burst than an indication of the intrinsic rarity or geometric uniqueness allowing for such a late break.

We also investigated the late-time ($t > 80$ days) optical behavior of long GRBs. We search for late-time ($t > 80$ day) optical light curves for a subsample of long GRBs that are comparable to GRB 221009A. We start with GRBs that are similarly highly energetic and include the 14 GRBs listed in E. Burns et al. (2023) with $E_{iso} > 2.5 \times 10^{54}$ erg (see their Table 4). We add to this the three GRBs with detected very-high-energy (VHE) emission, GRBs 180720B (H. Abdalla et al. 2019), 190114C (MAGIC Collaboration et al. 2019a, 2019b), and 190829A (H. E. S. S. Collaboration et al. 2021). Finally, we add to this the sample of four GRBs presented in J. C. Rastinejad et al. (2024): GRBs 030329, 100316D, 130427A, and 190829A, though we note that 190829A was already included in the VHE sample. These GRBs were selected because they are close ($z < 0.4$), have a detected SN, and importantly have a well-populated $t > 30$ days optical light curve.

In the case of the four presented in J. C. Rastinejad et al. (2024), all but GRB 130427A are dominated by SN emission at $t = 4 - 100+$ days. Following the fading of the SN associated with GRB 130427A at $t \sim 250$ days, the light curve appears to follow the decay pre-SN, excluding the possibility of a break in the interim. GRB 221009A is therefore unique among objects with late-time optical data in that its light curve does not appear to be dominated by SN emission and has a $t \sim 50$ day break.

In a literature search, we do not find optical data at $t > 80$ days for the remainder of the GRBs in our comparison sample. We note that for the afterglow of GRB 160625B, B. B. Zhang et al. (2018) report R -band upper limits at $t \sim 58$ days (see their Figure 2), which was close to our “late-time” cutoff, and they find no evidence for a break. We also note that for the afterglow of GRB 110918A, D. D. Frederiks et al. (2013) present UVOT photometry to ~ 48 days and found no evidence for a break.

5. Conclusions and Future Work

We present HST and JWST imaging of the afterglow and host galaxy of GRB 221009A at $t > 185$ days post-trigger. We find, with high statistical significance, disagreement with the extension to late times of a simple power-law afterglow plus SN decay fit to early observations. We next consider an alternative SN plus afterglow decay model, which requires a break in the light curve. This simple broken power law plus SN model underpredicts the latest F814W observations (Figure 6), which necessitates the addition of a secondary flux component in filters blueward of F160W. In statistical AIC and BIC tests, we disfavor all models except the broken power law plus SN plus constant model, and we find these results are not sensitive to our choice of measurement for V1 F160W (see Section 3.2). In the model requiring the constant component, we find support for $t_{brk} \sim 50 \pm 10$ days, which can be interpreted as a jet break assuming $\nu_m < \nu_c$ and $p > 2$, consistent with the results presented in T. Laskar et al. (2023). The modeling also indicates SN 2022xiw having an optical/NIR flux $< 1.4 \times$ SN 1998bw.

In our analysis of the SED, we find evidence for a blue source in addition to the afterglow. For this source to be explained exclusively by a SN similar to SN 1998bw, it would need to be a factor of ~ 3 times more luminous than SN 1998bw. This is inconsistent with our upper scaling limit of < 1.4 . We instead interpret this source as a scattered-light echo. We find consistency with this interpretation, with the predicted F814W – F110W color of -0.45 mag to -0.08 mag

in agreement with our measured color of -0.31 ± 0.21 mag. If confirmed, this would be the first detection of an optical scattered-light echo of a GRB afterglow. In an alternative interpretation, the presence of strong molecular hydrogen emission at the location of the GRB (P. K. Blanchard et al. 2024) lends support to the hypothesis that this source could be a young star cluster. Under these assumptions of $Z = 0.12 Z_{\odot}$, $m_{F110W} = 24.84$ mag, and age 1–4 Myr, we find a cluster with a mass of $M_* \sim 3 \times 10^5 M_{\odot}$. This mass is a factor of $\sim 10^2$ greater than masses of similarly young clusters in the SMC. If confirmed, this would be one of the most massive young clusters in a low-SFR environment.

Assuming a continued power-law decay with $\alpha = 2.34$, the afterglow should fade below the HST and JWST detection limits within the next \sim year. Continued monitoring of this source in the filters presented here will provide the observations necessary to better constrain the nature of the additional source. In later-time light curves, a light echo is expected to appear as a fading blue source, while a star cluster or dwarf satellite galaxy is expected to appear as a constant source in all wavelengths (though brightest in the bluest filters).

Template imaging will be crucial in robustly separating the host galaxy and diffraction spike light from the transient light. While observations in the HST and JWST bands will be helpful in better analyzing the early optical and NIR data, to fully understand GRB 221009A a full multiwavelength analysis with all epochs of data will be necessary.

Acknowledgments

We thank the anonymous referee for comments which improved this manuscript. We thank Wen-fai Fong, Charlie Kilpatrick, and Jay Strader for valuable conversations regarding this manuscript. We thank Jenni Barnes, Yvette Cendes, Dan Kasen, Joel Leja, Dan Siegel, and S. Karthik Yadavalli for significant contributions to the proposals which provided these data. This research made use of Photutils, an Astropy package for detection and photometry of astronomical sources (L. Bradley et al. 2023). T.E. is supported by NASA through the NAS. Hubble Fellowship grant No. HST-HF2-51504.001-A awarded by the Space Telescope Science Institute, which is operated by the Association of Universities for Research in Astronomy, Inc., for NASA, under contract NAS5-26555. W.J-G is supported by NASA through the NAS. Hubble Fellowship grant No. HST-HF2-51558.001-A awarded by the Space Telescope Science Institute, which is operated by the Association of Universities for Research in Astronomy, Inc., for NASA, under contract NAS5-26555. B.D.M. acknowledges support from NASA through the Astrophysics Theory Program (grant No. AST-2406637) and the Simons Investigator Program (grant No. 727700). The Flatiron Institute is supported by the Simons Foundation. Support for program GO-17278 was provided by NASA through a grant from the Space Telescope Science Institute, which is operated by the Association of Universities for Research in Astronomy, Inc., under NASA contract NAS 5-26555. Support for program DD-2784 was provided by NASA through a grant from the Space Telescope Science Institute, which is operated by the Association of Universities for Research in Astronomy, Inc., under NASA contract NAS 5-03127. The data were obtained from the Mikulski Archive for Space Telescopes at the Space Telescope Science Institute, which is operated by the Association of Universities for

Research in Astronomy, Inc., under NASA contract NAS 5-03127 for JWST. This research has made use of the NASA/IPAC Extragalactic Database (NED), which is funded by the National Aeronautics and Space Administration and operated by the California Institute of Technology.

Facilities: HST (WFC3), JWST (NIRCam).

Software: Astrodrizzle (S. L. Hoffmann et al. 2021), Astropy (Astropy Collaboration et al. 2013, 2018, 2022), Corner (D. Foreman-Mackey 2016), GALFIT (C. Y. Peng et al. 2010), HOTPANTS (A. Becker 2015), Matplotlib (J. D. Hunter 2007), Numpy (C. R. Harris et al. 2020), Photutils (L. Bradley et al. 2023), Source Extractor (E. Bertin & S. Arnouts 1996).

ORCID iDs

Huei Sears  <https://orcid.org/0000-0001-8023-4912>
 Ryan Chornock  <https://orcid.org/0000-0002-7706-5668>
 Peter K. Blanchard  <https://orcid.org/0000-0003-0526-2248>
 Raffaella Margutti  <https://orcid.org/0000-0003-4768-7586>
 V. Ashley Villar  <https://orcid.org/0000-0002-5814-4061>
 Justin Pierel  <https://orcid.org/0000-0002-2361-7201>
 Patrick J. Valley  <https://orcid.org/0000-0001-5661-7155>
 Kate D. Alexander  <https://orcid.org/0000-0002-8297-2473>
 Edo Berger  <https://orcid.org/0000-0002-9392-9681>
 Tarraneh Eftekhari  <https://orcid.org/0000-0003-0307-9984>
 Wynn V. Jacobson-Galán  <https://orcid.org/0000-0003-1103-3409>
 Tanmoy Laskar  <https://orcid.org/0000-0003-1792-2338>
 Natalie LeBaron  <https://orcid.org/0000-0002-2249-0595>
 Brian D. Metzger  <https://orcid.org/0000-0002-4670-7509>
 Dan Milisavljevic  <https://orcid.org/0000-0002-0763-3885>

References

Abbott, B. P., Abbott, R., Abbott, T. D., et al. 2017, *ApJL*, 848, L12
 Abdalla, H., Adam, R., Aharonian, F., et al. 2019, *Natur*, 575, 464
 Ajello, M., Arimoto, M., Axelsson, M., et al. 2019, *ApJ*, 878, 52
 Akaike, H. 1974, *ITAC*, 19, 716
 An, Z.-H., Antier, S., Bi, X.-Z., et al. 2023, arXiv:2303.01203
 Andrae, R., Schulze-Hartung, T., & Melchior, P. 2010, arXiv:1012.3754
 Astropy Collaboration, Price-Whelan, A. M., Lim, P. L., et al. 2022, *ApJ*, 935, 167
 Astropy Collaboration, Price-Whelan, A. M., Sipőcz, B. M., et al. 2018, *AJ*, 156, 123
 Astropy Collaboration, Robitaille, T. P., Tollerud, E. J., et al. 2013, *A&A*, 558, A33
 Becker, A. 2015, OTPANTS: High Order Transform of PSF ANd Template Subtraction, Astrophysics Source Code Library, ascl:1504.004
 Bertin, E., & Arnouts, S. 1996, *A&AS*, 117, 393
 Blanchard, P., Chornock, R., Villar, A., et al. 2022, JWST Proposal. Cycle 1, ID. #2784
 Blanchard, P. K., Berger, E., & Fong, W.-f. 2016, *ApJ*, 817, 144
 Blanchard, P. K., Villar, V. A., Chornock, R., et al. 2024, *NatAs*, 8, 774
 Bloom, J. S., Frail, D. A., & Kulkarni, S. R. 2003, *ApJ*, 594, 674
 Bradley, L., Sipőcz, B., Robitaille, T., et al. 2023, astropy/photutils: v1.8.0, Zenodo, doi:10.5281/zenodo.7946442
 Bright, J. S., Rhodes, L., Farah, W., et al. 2023, *NatAs*, 7, 986
 Burnham, K. P., & Anderson, D. R. 2004, *Sociological Methods & Research*, 33, 261
 Burns, E., Svirsin, D., Fenimore, E., et al. 2023, *ApJL*, 946, L31
 Calabro, A., Amorin, R., Fontana, A., et al. 2017, *A&A*, 601, A95
 Chevalier, R. A. 1986, *ApJ*, 308, 225
 Chevalier, R. A., & Li, Z.-Y. 2000, *ApJ*, 536, 195
 Chornock, R., Alexander, K. D., Berger, E., et al. 2022, HST Proposal. Cycle 30, ID. #17278
 Cikota, A., Ding, J., Wang, L., et al. 2023, *ApJL*, 949, L9
 Clocchiatti, A., Suntzeff, N. B., Covarrubias, R., & Candia, P. 2011, *AJ*, 141, 163
 Conroy, C., & Gunn, J. E. 2010, *ApJ*, 712, 833
 Conroy, C., Gunn, J. E., & White, M. 2009, *ApJ*, 699, 486
 Conroy, C., White, M., & Gunn, J. E. 2010, *ApJ*, 708, 58
 Crotts, A. P. S. 2015, *ApJL*, 804, L37
 Crotts, A. P. S., Kunkel, W. E., & Heathcote, S. R. 1995, *ApJ*, 438, 724
 D'Avanzo, P., Ferro, M., Brivio, R., et al. 2022, GCN, 32755, 1
 de Ugarte Postigo, A., Izzo, L., Pugliese, G., et al. 2022a, GCN, 32648, 1
 de Ugarte Postigo, A., Izzo, L., Thoene, C. C., et al. 2022b, GCN, 32800, 1
 Della Valle, M., Chincarini, G., Panagia, N., et al. 2006, *Natur*, 444, 1050
 Dichiara, S., Groppi, J. D., Kennea, J. A., et al. 2022, GCN, 32632, 1
 Fitzpatrick, E. L. 1999, *PASP*, 111, 63
 Foreman-Mackey, D. 2016, *JOSS*, 1, 24
 Foreman-Mackey, D., Hogg, D. W., Lang, D., & Goodman, J. 2013, *PASP*, 125, 306
 Frail, D. A., Kulkarni, S. R., Sari, R., et al. 2001, *ApJL*, 562, L55
 Frederiks, D. D., Hurley, K., Svirsin, D. S., et al. 2013, *ApJ*, 779, 151
 Frederiks, D., Svirsin, D., Lysenko, A. L., et al. 2023, *ApJL*, 949, L7
 Fruchter, A. S., Levan, A. J., Strolger, L., et al. 2006, *Natur*, 441, 463
 Fulton, M. D., Smartt, S. J., Rhodes, L., et al. 2023, *ApJL*, 946, L22
 Fynbo, J. P. U., Watson, D., Thöne, C. C., et al. 2006, *Natur*, 444, 1047
 Gal-Yam, A., Fox, D. B., Price, P. A., et al. 2006, *Natur*, 444, 1053
 Galama, T. J., Vreeswijk, P. M., van Paradijs, J., et al. 1998, *Natur*, 395, 670
 Gao, H., Lei, W.-H., Zou, Y.-C., Wu, X.-F., & Zhang, B. 2013, *NewAR*, 57, 141
 Gehrels, N., Norris, J. P., Barthelmy, S. D., et al. 2006, *Natur*, 444, 1044
 Ghisellini, G., Ghirlanda, G., Mereghetti, S., et al. 2006, *MNRAS*, 372, 1699
 Gillanders, J. H., Troja, E., Fryer, C. L., et al. 2023, arXiv:2308.00633
 Gompertz, B. P., Ravasio, M. E., Nicholl, M., et al. 2023, *NatAs*, 7, 67
 Gordon, K. D., Clayton, G. C., Decler, M., et al. 2023, *ApJ*, 950, 86
 Guarini, E., Tamborra, I., Bégué, D., & Rudolph, A. 2023, *MNRAS*, 523, 149
 H. E. S. S. Collaboration, Abdalla, H., Aharonian, F., et al. 2021, *Sci*, 372, 1081
 Harris, C. R., Millman, K. J., van der Walt, S. J., et al. 2020, *Natur*, 585, 357
 Hoffmann, S. L., Mack, J., Avila, R., et al. 2021, AAS Meeting, 53, 216.02
 Hollyhead, K., Bastian, N., Adamo, A., et al. 2015, *MNRAS*, 449, 1106
 Huang, Y., Hu, S., Chen, S., et al. 2022, GCN, 32677, 1
 Hunter, D. A., Elmegreen, B. G., Dupuy, T. J., & Mortonson, M. 2003, *AJ*, 126, 1836
 Hunter, J. D. 2007, *CSE*, 9, 90
 Kong, D.-F., Wang, X.-G., Zheng, W., et al. 2024, *ApJ*, 971, 56
 Laskar, T., Alexander, K. D., Margutti, R., et al. 2023, *ApJL*, 946, L23
 Lesage, S., Veres, P., Briggs, M. S., et al. 2023, *ApJL*, 952, L42
 Levan, A. J., Barclay, T., Bernardini, M. G., et al. 2022, HST Proposal. Cycle 30, ID. #17264
 Levan, A. J., Gompertz, B. P., Salafia, O. S., et al. 2024, *Natur*, 626, 737
 Levan, A. J., Lamb, G. P., Schneider, B., et al. 2023, *ApJL*, 946, L28
 LHAASO Collaboration, Cao, Z., Aharonian, F., et al. 2023, *Sci*, 380, 1390
 Lyman, J. D., Levan, A. J., Tanvir, N. R., et al. 2017, *MNRAS*, 467, 1795
 MAGIC Collaboration, Acciari, V. A., Ansoldi, S., et al. 2019a, *Natur*, 575, 455
 MAGIC Collaboration, Acciari, V. A., Ansoldi, S., et al. 2019b, *Natur*, 575, 459
 Maiorano, E., Palazzi, E., Rossi, A., et al. 2022, GCN, 32850, 1
 Malesani, D. B., Levan, A. J., Izzo, L., et al. 2023, *A&A*, in press (arXiv:2302.07891)
 Melandri, A., Covino, S., Rogantini, D., et al. 2014, *A&A*, 565, A72
 Michałowski, M. J., Xu, D., Stevens, J., et al. 2018, *A&A*, 616, A169
 Miller, A. A., Smith, N., Li, W., et al. 2010, *AJ*, 139, 2218
 Nava, L., Salvaterra, R., Ghirlanda, G., et al. 2012, *MNRAS*, 421, 1256
 Negro, M., Di Lalla, N., Omodei, N., et al. 2023, *ApJL*, 946, L21
 O'Connor, B., Troja, E., Ryan, G., et al. 2023, *SciA*, 9, eadi1405
 Ofek, E. O., Cenko, S. B., Gal-Yam, A., et al. 2007, *ApJ*, 662, 1129
 Peng, C. Y., Ho, L. C., Impey, C. D., & Rix, H.-W. 2010, *AJ*, 139, 2097
 Raftery, A. E. 1995, *Sociol. Method*, 25, 111
 Rastinejad, J. C., Fong, W., Levan, A. J., et al. 2024, *ApJ*, 968, 14
 Rastinejad, J. C., Gompertz, B. P., Levan, A. J., et al. 2022, *Natur*, 612, 223
 Ren, J., Wang, Y., Zhang, L.-L., & Dai, Z.-G. 2023, *ApJ*, 947, 53
 Rhoads, J. E. 1999, *ApJ*, 525, 737
 Rhodes, L., van der Horst, A. J., Bright, J. S., et al. 2024, *MNRAS*, 533, 4435
 Sari, R., Piran, T., & Halpern, J. P. 1999, *ApJL*, 519, L17
 Sato, Y., Murase, K., Ohira, Y., & Yamazaki, R. 2023, *MNRAS*, 522, L56
 Schlaflay, E. F., & Finkbeiner, D. P. 2011, *ApJ*, 737, 103
 Schmidt, B. P., Kirshner, R. P., Leibundgut, B., et al. 1994, *ApJL*, 434, L19
 Schwarz, G. 1978, *AnSta*, 6, 461
 Shrestha, M., Sand, D. J., Alexander, K. D., et al. 2023, *ApJL*, 946, L25
 Smith, N., Foley, R. J., Bloom, J. S., et al. 2008, *ApJ*, 686, 485

Srinivasaragavan, G. P., O'Connor, B., Cenko, S. B., et al. 2023, *ApJL*, **949**, L39
Svensson, K. M., Levan, A. J., Tanvir, N. R., Fruchter, A. S., & Strolger, L. G. 2010, *MNRAS*, **405**, 57
Tak, D., Uhm, Z. L., Paek, G. S. H., et al. 2025, *ApJ*, **978**, 29
Tanga, M., Krühler, T., Schady, P., et al. 2018, *A&A*, **615**, A136
Troja, E., Fryer, C. L., O'Connor, B., et al. 2022, *Natur*, **612**, 228
Tsvetkova, A., Frederiks, D., Golenetskii, S., et al. 2017, *ApJ*, **850**, 161
van den Bergh, S. 2006, *AJ*, **131**, 1559
Veres, P., Burns, E., Bissaldi, E., et al. 2022, GCN, **32636**, 1
Verma, A., Sharma, S., Dewangan, L. K., et al. 2024, *AJ*, **168**, 98
Virgili, F. J., Liang, E.-W., & Zhang, B. 2009, *MNRAS*, **392**, 91
Wang, X.-G., Zhang, B., Liang, E.-W., et al. 2018, *ApJ*, **859**, 160
Wang, Y.-Z., Huang, Y.-J., Liang, Y.-F., et al. 2017, *ApJL*, **851**, L20
Williams, M. A., Kennea, J. A., Dichiara, S., et al. 2023, *ApJL*, **946**, L24
Woosley, S. E., & Bloom, J. S. 2006, *ARA&A*, **44**, 507
Yang, Y., Wang, L., Baade, D., et al. 2018, *ApJ*, **852**, 89
Yang, Y.-H., Troja, E., O'Connor, B., et al. 2024, *Natur*, **626**, 742
Yi, S.-X., Wu, X.-F., Wang, F.-Y., & Dai, Z.-G. 2015, *ApJ*, **807**, 92
Zhang, B. B., Zhang, B., Castro-Tirado, A. J., et al. 2018, *NatAs*, **2**, 69
Zhao, W., Zhang, J.-C., Zhang, Q.-X., et al. 2020, *ApJ*, **900**, 112